Scanning micro-Hall probe mapping of magnetic flux distributions and current densities in $YBa_2Cu_3O_7$ thin films

W. Xing,[a] B. Heinrich,[a] Hu Zhou,[b] A.A. Fife,[b] A.R. Cragg,[b] and P.D. Grant[c]

[a] Department of Physics, Simon Fraser University, Burnaby, B.C. Canada V5A 1S6
[b] CTF Systems Inc., 15-1750 McLean Avenue, Port Coquitlam, B.C. Canada V3C 1M9
[c] National Research Council of Canada, Ottawa, Canada K1A 0R6

Mapping of the magnetic flux density B_z (perpendicular to the film plane) for a $YBa_2Cu_3O_7$ thin-film sample was carried out using a scanning micro-Hall probe. The sheet magnetization and sheet current densities were calculated from the B_z distributions. From the known sheet magnetization, the tangential ($B_{x,y}$) and normal components of the flux density **B** were calculated in the vicinity of the film. It was found that the sheet current density was mostly determined by $2B_{x,y}/d$, where d is the film thickness. The evolution of flux penetration as a function of applied field will be shown.

PACS numbers: 74.60.Jg, 74.75.+t

I. Introduction

Stationary and scanning Hall probes have been used for evaluation of high temperature superconducting (HTS) thin films.[1-4] The magnetic flux density B_z normal to the film surface is usually measured. Algorithms were developed[4-7] to calculate the sheet current density **J** from the measured field above the sample (inverse problem). In our previous paper,[4] the inverse problem was converted to a magnetostatic calculation using

$$\mathbf{J} = \nabla \times \mathbf{M} = \left(J_x, J_y\right) = \left(\frac{\partial M}{\partial y}, -\frac{\partial M}{\partial x}\right). \quad (1)$$

where the sheet magnetization M is normal to the film plane (parallel to z-axis).

The flux density B_z at the point (m,n,z) is given by[8]

$$B_z = \sum_{i,j=1}^{N1,N2} \frac{\mu_0}{4\pi} M(i,j) \int_{S_{i,j}} \frac{3z^2 - r^2}{r^5} dx'\, dy' = \sum_{i,j=1}^{N1,N2} M(i,j) G(m,n,i,j,z) \quad (2)$$

where r is the distance between the local sheet magnetization M(i,j) and the field point (m,n,z). N1 and N2 are the total number of scanning steps in the x and y directions, respectively. The integral in (2) is over the area of the grid cell (i,j). Equation (2) can be written in matrix notation[4]

$$\mathbf{B_z} = \mathbf{G} \cdot \mathbf{M}. \quad (3)$$

where G is a matrix of order of $N_1^2 \times N_2^2$ and M and B_z are column vectors of dimensions $N1 \times N2$. Equation (3) states that the sheet magnetization is uniquely determined by the measured $B_z(x,y)$. The sheet magnetization M(i,j) allows one to calculate the flux density **B** anywhere around the film including the tangential components $B_{x,y}$ of **B**, which are not obtainable directly from our scanning Hall Probe measurements. That way one can obtain a full picture of the flux penetration. This is a forward problem which does not require the time consuming solutions of inverse matrixes.

The contributions to **J** from the gradient of B and from the curvature of **B** were compared. The purpose of this paper is to illustrate graphically the evolution of flux penetration into a zero-field-cooled $YBa_2Cu_3O_7$ (YBCO) thin-film sample.

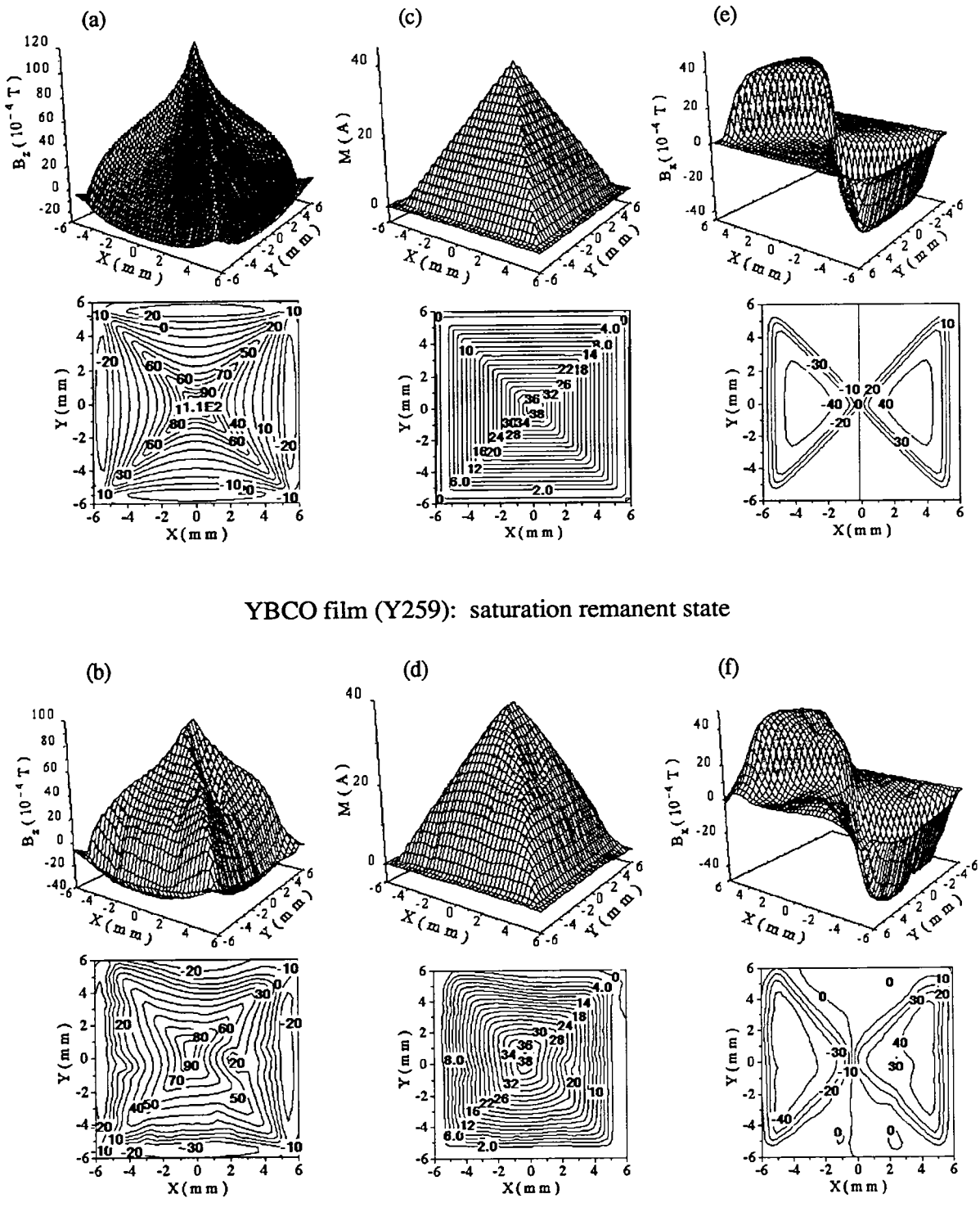

Fig. 1. (a) and (b) B_z, (c) and (d) M, and (e) and (f) B_x distributions in the remanent state for an ideal film with uniform current distributions and for a YBCO thin film (sample Y259), respectively.

II. Experimental

The micro-Hall probe was patterned from a GaAs quantum-well heterostructure thin film (University of Bath). Its active area is 25 × 25 μm. The scanning micro-Hall probe system is a customized commercial device developed by Quantum Technology Corp.[9] in collaboration with the participants from Simon Fraser University. Epitaxial quality YBCO thin-film samples were prepared on $LaAlO_3$ substrates by pulsed excimer laser ablation from a stoichiometric target of YBCO. We present the data for one of the YBCO films (Y259) in this paper. Sample Y259 had a critical temperature of 90 K, and lateral dimensions ≈ 1.08 × 1.08 cm, and thickness d ≈ 300 nm. The Hall probe was maintained at a constant height of z ≈ 250 μm above the film surface while taking the lateral scans. The lateral scanning step was 0.3 mm. The experimental details can be found in Ref. 4.

III. Results and discussion

Fig. 1 compares the theoretical calculations for an ideal film (uniformly distributed currents flowing in concentric square paths) with the measurement results for the YBCO (Y259) thin film. Figs. 1(a) and 1(b) show the B_z distributions for the ideal film and for the YBCO film, respectively. An external field H_a ($\mu_0 H_a \approx 30$ mT) perpendicular to the film plane was applied to the YBCO film (zero-field-cooled), and then H_a was switched off. The mapping of B_z was carried out with the film in a remanent state. The applied flux B_a penetrated fully into the film. The ideal film was chosen to have the same size as that of sample Y259. The sheet current for the ideal sample, j (= J/d) = 2.5 × 10^6 A/cm^2, was chosen to bring the overall dependence of B_z close to that of the YBCO sample. The distribution of M(x,y) was obtained by solving the matrix equations (2).[4] The results are shown in Figs. 1(c) and 1(d). Fig. 1(d) demonstrates that the YBCO sample was in the saturated state. The contour lines of M(x,y) represent the current stream lines, and the separation between stream

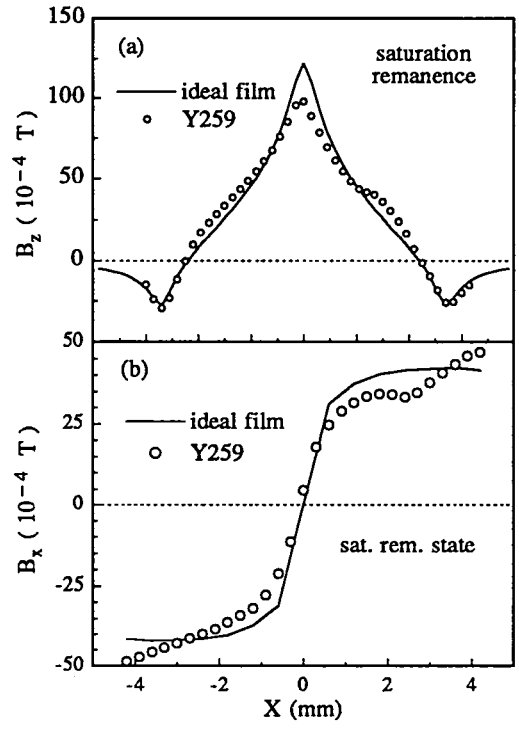

Fig. 2. (a) $B_z(x)$ and (b) $B_x(x)$ for y = 0 in the saturation remanent state; the open circles are $B_{x,z}$ values for the YBCO film and the solid lines for the ideal film.

lines is inversely proportional to the value of the sheet current density [Eq. (1)].

B_x and B_y at point (m,n,z) are given by

$$B_{x,y} = \sum_{i,j=1}^{N1,N2} \frac{\mu_0}{4\pi} M(i,j) \cdot \int_{S_{i,j}} \frac{3x(\text{or } y)z}{r^5} dx'\, dy' . \qquad (4)$$

Figs. 1(e) and 1(f) show that $B_x(x,y)$ is distributed over two opposing triangles. The sample symmetry requires that the component B_y is distributed in two other triangles. In each triangular region, there are either $B_{x,z}$ or $B_{y,z}$ components of **B**. B_x and B_y vanish along the film diagonals.

The distributions of B_x, B_z, and M for the YBCO film are very similar to those of the ideal film. However there are noticeable deviations of the flux distribution from the four-fold symmetry pattern which are caused by defects in the YBCO sample, see Figs. 1 and 2.

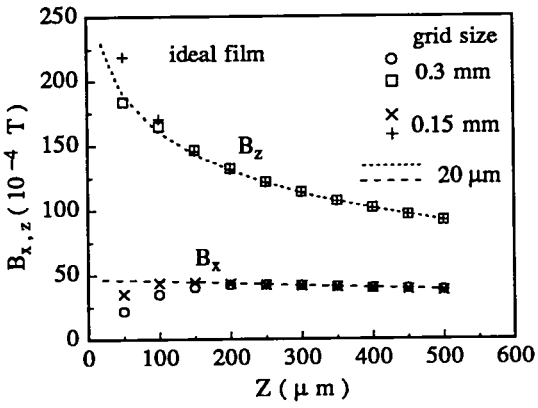

Fig. 3. Calculated $B_{x,z}$ values versus z for the ideal film for different grid size of the sheet magnetization M(x,y).

The calculations in Fig. 3 were used to demonstrate the dependence of B_x and B_z on the grid size, w, of the sheet magnetization M(x,y). B_z was calculated at the film center. B_x was calculated at midway between the center and the edge of the film. The calculated values of B_x are correct if the distance above the sample surface $z \geq w$. B_x decreases for $z < w$ and reaches zero when $z \rightarrow 0$. This is an artifact of the finite grid size. In an ideal sample B_x should reach a constant value by approaching the film surface (Ampere's law). The decrease in B_x for $z < w$ is due to the change of the sign of B_x across the mid-plane of the film. The calculated values of B_z support that view. B_z is continuous across the film thickness and the calculated B_z show no noticeable dependence on w.

The application of Ampere's Law

$$\oint \mathbf{B} \cdot d\mathbf{l} = \mu_0 I \qquad (5)$$

to a path in x-z plane shown in Fig. 4 leads to

$$\frac{\Delta B_x}{d} + \frac{\Delta B_z}{\ell}\frac{t}{d} = \mu_0 j_y, \qquad (6)$$

where ℓ and t are the integral paths along the x and z directions and ΔB_z is the difference in the B_z components which are separated laterally by ℓ. ΔB_x is the difference between the B_x components above and below the

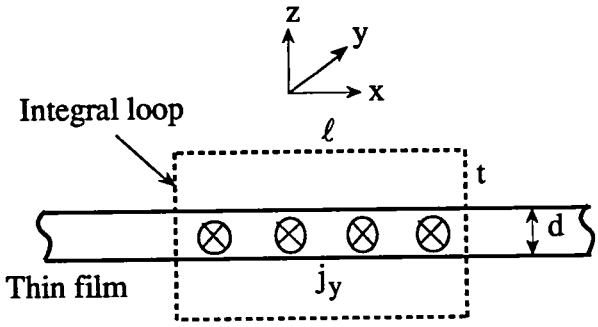

Fig. 4. Schematic diagram of the integral path for the application of Ampere's law.

film, see Fig. 4. Since d is comparable to 2λ, where λ is the London penetration depth, j is considered uniform over the film thickness. (Otherwise, j is the average value over the film thickness.) The first term in (6) is due to the curvature of **B**, ($B\nabla \times \hat{\mathbf{B}}$, where $\hat{\mathbf{B}}$ is the unit vector along $\mathbf{B} = B\hat{\mathbf{B}}$) and the second term is due to the gradient of B, ($\nabla B \times \hat{\mathbf{B}}$).[10] Since B_x and B_z are comparable and t can be close to d, the flux gradient term is much smaller (by approximately three orders of magnitude) than the flux curvature term. In other words, j is mostly determined by the curvature term,

$$\frac{\Delta B_{x,y}}{d} = \frac{2B_{x,y}}{d} = \mu_0 |j_{y,x}|. \qquad (7)$$

This observation is in agreement with the theoretical analysis of Clem.[10] From Eq. (7) and from the local sheet current $j_c = 3 \times 10^6$ A/cm^2 corresponding to $x \approx -5$ mm in Fig. 2, it can be shown that the calculated value of B_x (for z=250 μm) is 13% smaller than that obtained from Eq. (7). In fact, the profile of the $B_x(x)$ curve in Fig. 2(b) is very similar to that of $j_y(x)$ for the YBCO film.[4] This shows clearly that the local current density in superconducting thin films determines the parallel components of **B** in the vicinity of the film. Fig 2(b) shows that B_x does not reach the saturated value as in the case of an ideal sample. The observed slope of B_x in Fig. 2(b) is a consequence of the dependence of j_c on the local B_z, see Ref. 4.

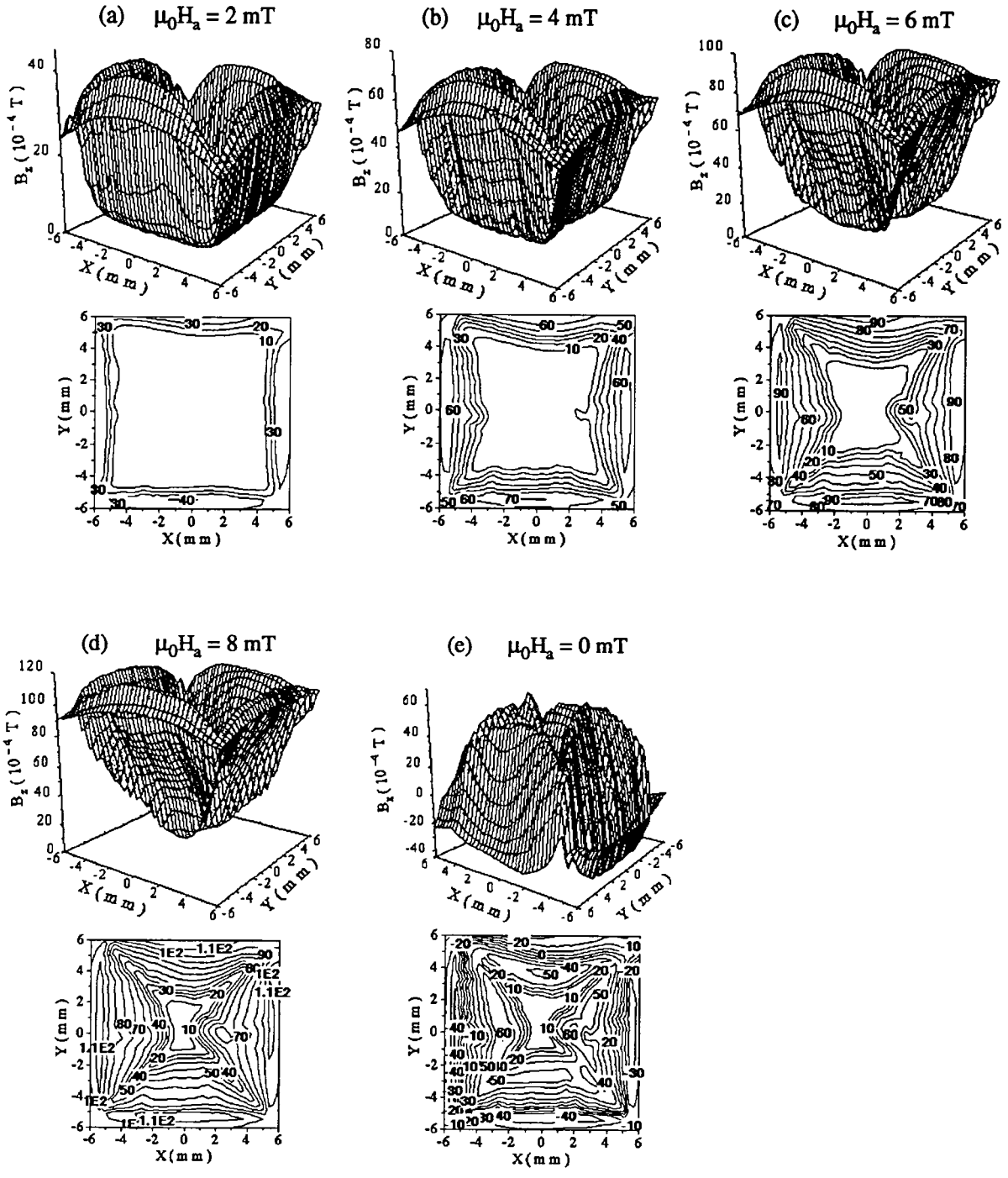

Fig. 5. Measured B_z of the YBCO film for $\mu_0 H_a$ = (a) 2 mT, (b) 4 mT, (c) 6 mT, (d) 8 mT, and (e) 0 mT.

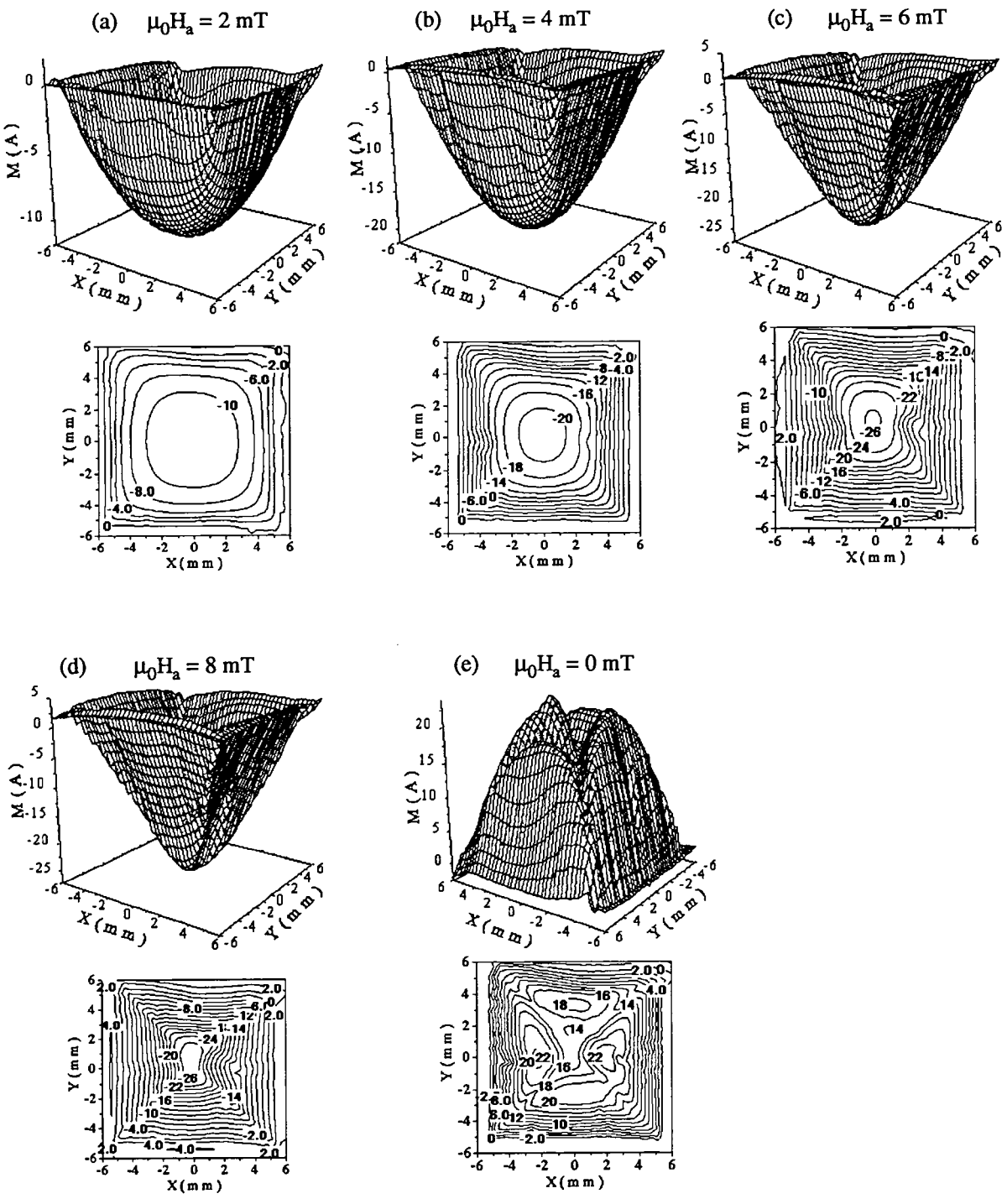

Fig. 6. The sheet magnetization M of the YBCO film for $\mu_0 H_a$ = (a) 2 mT, (b) 4 mT, (c) 6 mT, (d) 8 mT, and (e) zero mT.

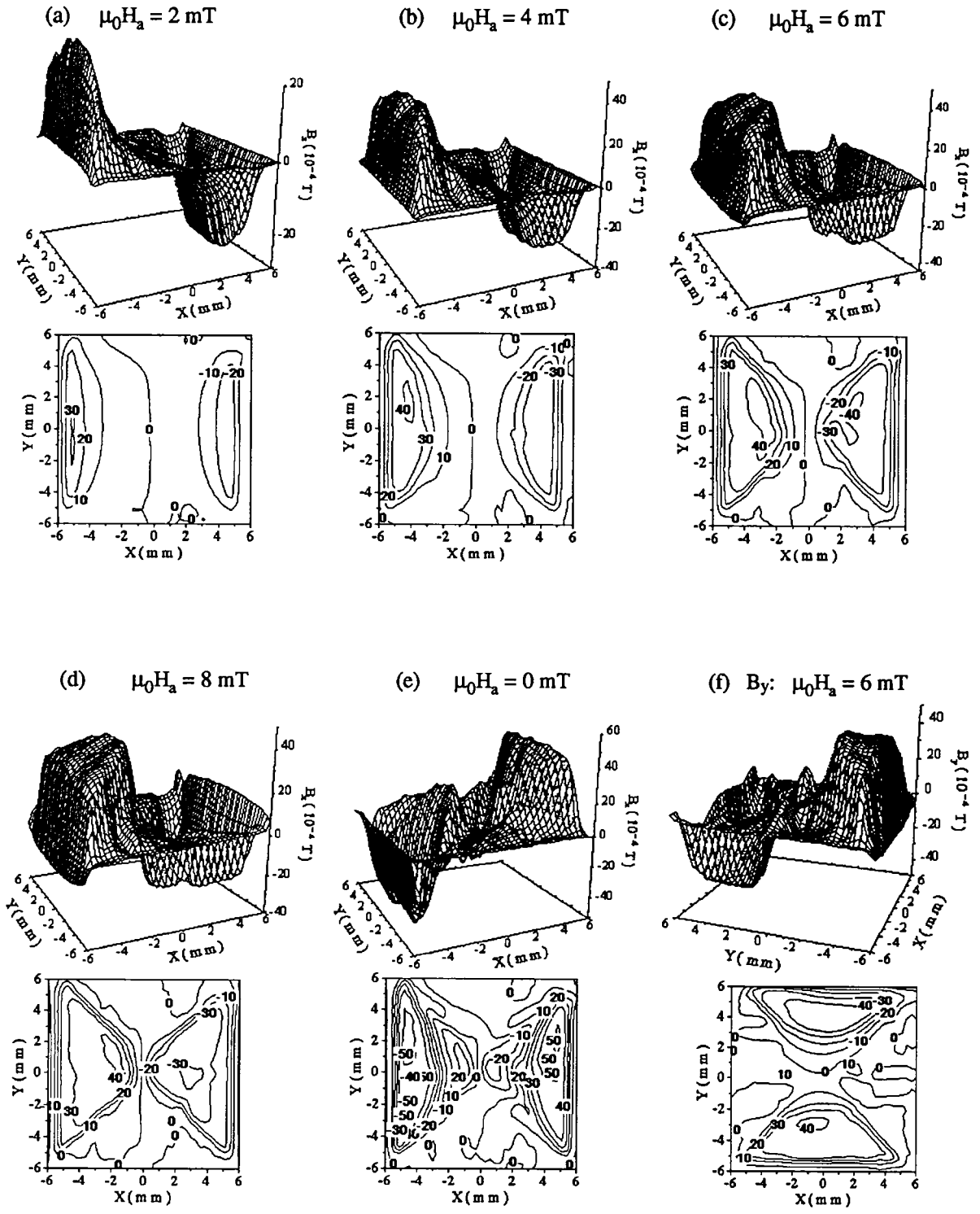

Fig. 7. B_x of the YBCO film for $\mu_0 H_a$ = (a) 2 mT, (b) 4 mT, (c) 6 mT, (d) 8 mT, and (e) 0 mT; (f) B_y for $\mu_0 H_a$ = 6 mT.

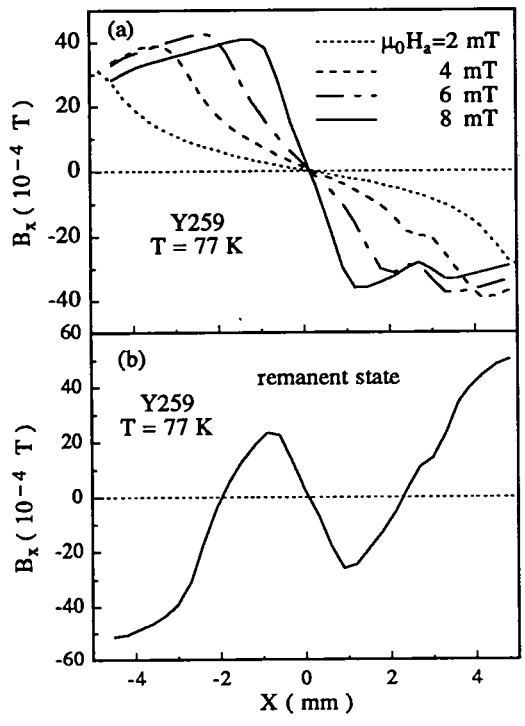

Fig. 8. B_x versus x for the YBCO film (a) in different applied fields (b) in a remanent state.

Figs. 5-8 show B_z, M, and B_x distributions for sequentially applied external fields. Fig. 9 shows vector field plots of the total flux density **B** in the x-z plane at y = 0 for various final states, described in the figure caption. The evolution of flux penetration and the corresponding current distributions can be best viewed by the combination of Figs. 5-9.

Fig. 7(f) shows the non-zero values of B_y over the region where B_x should dominate. This non-symmetrical flux distribution is due to the presence of a defect which is centered around x=3, y=0, see Fig. 5(c). Fig. 5(c) shows that the sheet current path curves around this defect and that causes a simultaneous presence of the B_x and B_y components in that region.

Figs. 9(a) and 9(b) show the saturation remanent flux distributions for the ideal and the YBCO films, respectively. The return flux (pointing in $-\hat{z}$ direction) results in the demagnetizing field around the film edge. The magnitude of **B** decreases rapidly away from the film surface.

Figs. 5-9 show that for relatively low applied fields (e.g. μ_0H_a = 2 mT), the induced supercurrents effectively shield the interior of the film from the external flux B_a. However, the tangential components $B_{x,y}$ are present over the entire film surface. The exclusion of B_z requires screening currents across the whole film surface,[4] and the presence of $B_{x,y}$ in vortex-free region is a consequence of Ampere's law. However note that the values of $B_{x,y}$ in the vortex-free region are smaller than those in the vortex-penetrated regions [corresponding to the plateaus in $B_x(x,y)$ in Fig. (7)] where the supercurrent reached its critical value, see Fig. 8.

Fig. 9(c) shows a noticeable bending of the flux lines over the film surface. The Lorentz force density $\mathbf{F} = \mathbf{j} \times \mathbf{B}$ has two components. The tangential component (due to B_z) points inwards and is responsible for moving the flux lines; this force density is balanced by the pinning force density. The perpendicular component (due to $B_{x,y}$) points downwards at the top and upwards at the bottom of the film. This part of the Lorentz force density causes the tilting of vortex lines.

It is interesting to note that the distortion of the applied flux is clearly visible only for $z \leq 5$ mm, see Fig. 9(c), which is approximately equal to the half length of the film edge.

As the applied field progressively increases, the flux penetrates deeper into the film and the region in which flux lines appreciably deviate from the external flux is more and more confined to the center of the film, see Figs. 9(d)-9(f);

Fig. 9(g) shows the flux line patterns in the remanent state after the applied field μ_0H_a = 8 mT was switched off. The trapped flux shows four hilltops, see Fig. 5(e). It is worthwhile to point out that at the hilltops (maxima of B_z) both $B_{x,y}$ and J are zero [Figs. 8, 9(b), and 9(g)]. The induced currents flow in closed loops under each hilltop and enclose the hilltops along the sample edges [Fig. 6(e)]. This multiply-connected current distribution can be reconstructed using a linear superposition principle with appropriate "virgin" states[11,4].

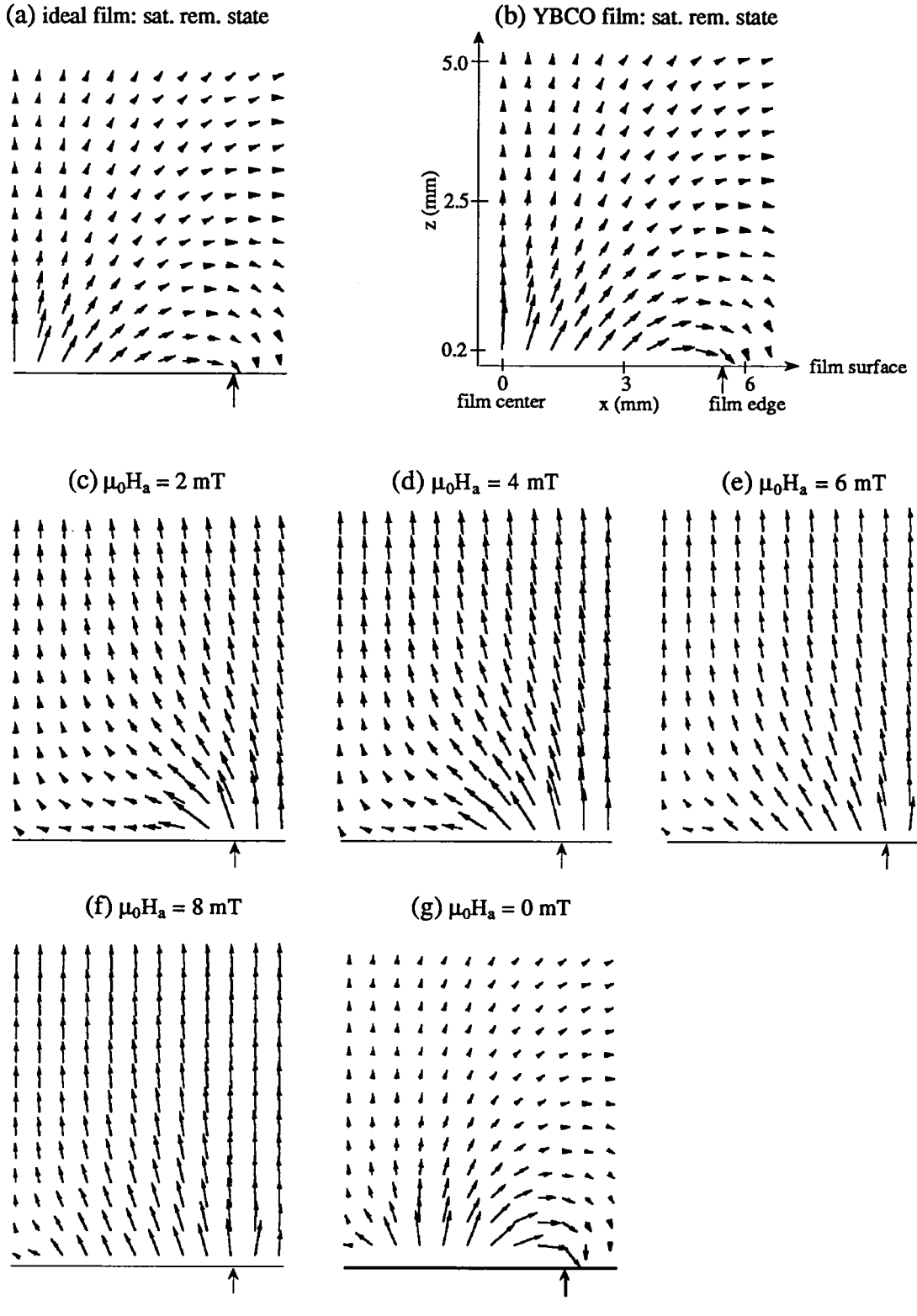

Fig. 9. Vector field plots of the flux density B in x-z plane (a) and (b) for the ideal and the YBCO films in the saturation remanent state, and for the YBCO film for $\mu_0 H_a$ = (c) 2 mT, (d) 4 mT, (e) 6 mT, (f) 8 mT, and (g) 0 mT.

IV. Conclusion

The mapping of B_z near the superconducting film surface is shown here to include complete and detailed information of the current distributions in the film, and the flux density in the film vicinity. The tangential components $B_{x,y}$ of the flux density **B** were calculated from the sheet magnetization M which was determined from the normal component of **B**, B_z. B_z was measured by a scanning micro-Hall probe. The minimum height at which the tangential components $B_{x,y}$ can be evaluated is determined by the scan step size. The application of Ampere's law indicates that the induced supercurrents in the YBCO thin-film sample are nearly entirely determined by $2B_{x,y}/d$, which is due to the curvature of **B**.

The Lorentz force has two components, one due to B_z, the other due to $B_{x,y}$. In the stationary state, the Lorentz force caused by B_z is compensated by the restoring force of pinning sites and the Lorentz force caused by the tangential flux densities $B_{x,y}$ is responsible for the tilting of flux lines. The calculation of **B** in the vicinity of the film revealed several interesting features: (a) the extent of screening by supercurrents in the vertical direction is comparable to that in the horizontal direction. With an increasing applied field, the flux penetrates deeper into the film and the region in which flux lines appreciably deviate from the external field is more and more confined to the center of the films; (b) in the remanent state, the areas with a maximum trapped flux density have no supercurrents; (c) the tangential components B_x and B_y are mostly present in separate and mutually perpendicular triangular regions. A significant presence of B_x and B_y in the same region, is a consequence of local defects; (d) the tangential flux densities B_x, B_y are nearly zero along the film diagonals.

Acknowledgments

We thank P.H. Brown and S. Govorkov for assistance in testing and assembling the measuring system. The assistance of S. Bending of University of Bath in providing the custom Hall probe is gratefully acknowledged.

This work was supported by the Natural Sciences and Engineering Research Council of Canada, Industry Canada (STP-AIM program), and the BC Ministry of Employment and Investment.

References

[1] M.J. Scharen, A.H. Cardona, J.Z. Sun, L.C. Bourne, and J.R. Schrieffer, Jpn. J. Appl. Phys., 30, L15 (1991).

[2] P. Brüll, D. Kirchgässner, and P. Leiderer, Physica C 182, 339 (1991).

[3] W. Rauch, H. Behner, and E. Gornik, Physica C 201, 179 (1992).

[4] W. Xing, B. Heinrich, Hu Zhou, A.A. Fife, and A.R. Cragg, submitted to J. of Appl. Phys., 1994.

[5] G.M. Asher, J.T. Williams, C.R. Walters, H. Joyce and R.J.A. Paul, IEEE Trans. Magn. 18, 540 (1982).

[6] B.J. Roth, N.G. Sepulveda, and J.P. Wikswo, J. Appl. Phys. 65, 361 (1989).

[7] P.D. Grant, M.W. Denhoff, W. Xing, P.H. Brown, S. Govorkov, I. Entin, J.C. Irwin, B. Heinrich, H. Zhou, A.A. Fife, and A.R. Cragg, submitted to Physica C, 1994.

[8] J. D. Jackson, Classical Electrodynamics, (Wiley, New York, 1975), Chap. 5.

[9] Quantum Technology Corp., 1370 Alpha Lake Road, Unit 15, Whistler, B.C. Canada V0N 1B1, Telephone: (604) 938-0030.

[10] John R. Clem, to be published in the Proc. of the 7th int. workshop on critical currents in superconductors, Jan. 24-27, 1994, Alpbach, Austria.

[11] E.H. Brandt, M. Indenbom, and A. Forkl, Europhys. Lett. 20, 735 (1993).